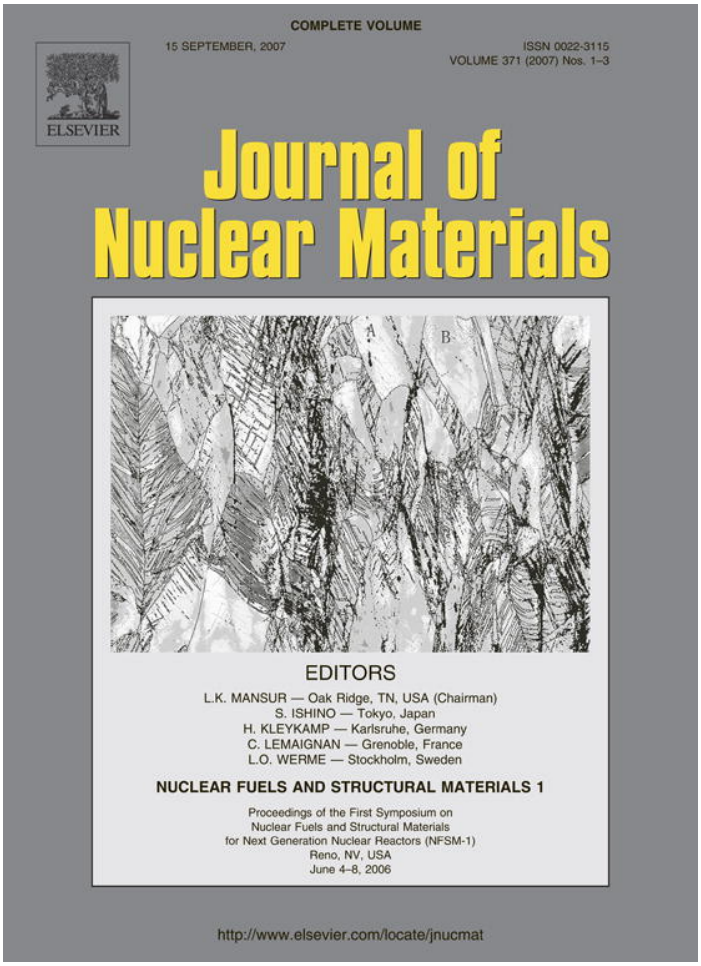

Available online at www.sciencedirect.com
ScienceDirect
Journal of Nuclear Materials 371 (2007) 61–75
journal of nuclear materials
www.elsevier.com/locate/jnucmat

Zirconium alloys for supercritical water reactor applications: Challenges and possibilities

Arthur T. Motta [a,*], Aylin Yilmazbayhan [a], Marcelo J. Gomes da Silva [a], Robert J. Comstock [b], Gary S. Was [c], Jeremy T. Busby [c], Eric Gartner [c], Qunjia Peng [c], Yong Hwan Jeong [d], Jeong Yong Park [d]

[a] *Department of Mechanical and Nuclear Engineering, 227 Reber Bldg. Penn State, University Park, PA 16802, USA*
[b] *Science and Technology Department, Westinghouse Electric Co., Pittsburgh, PA 15235-5082, USA*
[c] *Nuclear Engineering and Radiological Sciences, University of Michigan, 2355 Bonisteel Blvd., Ann Arbor, MI-48109, USA*
[d] *Zr Fuel Cladding Team, Korea Atomic Energy Research Institute, Daejeon 305-353, Republic of Korea*

Abstract

The corrosion behavior of model Zr-based alloys at 500 °C is assessed by long term (up to 400 days) corrosion testing in an effort to evaluate their potential for use in the supercritical water reactor and to assess the influence of alloying elements on corrosion behavior. The corrosion weight gains from such systematic testing are seen to be a factor of five higher than those measured at 360 °C but the protectiveness ranking of the alloys is similar. Detailed characterization of the oxide layers to rationalize the differences in corrosion behavior was performed using synchrotron radiation and systematic differences are observed in protective and non-protective oxides, especially near the oxide–metal interface. The overall corrosion rate of the best Zr-based alloys compared favorably with those of other alloys being considered for use in the supercritical water reactor.

PACS: 81.65.Kn; 61.10.Nz; 81.15.Aa; 68.55.Jk

1. Introduction

In the supercritical water reactor (SCWR), the fuel cladding and other core components are expected to operate at 500–550 °C and are to be subjected to a potentially corrosive environment [1]. Little knowledge exists of the behavior of materials under these conditions, but several candidate alloys are currently being tested for possible use in these reactors [2]. Zirconium alloys initially did not receive much consideration for these high temperature applications because it was thought that the corrosion rates would be too high, and that the materials would not be strong enough. However earlier work [3–5] indicated that some high alloying content Zr alloys showed promise for high temperature corrosion applications.

There are significant advantages associated with using a more neutron-transparent cladding material than the alloys currently envisaged for the SCWR (Inconels and steels), including decreasing the

* Corresponding author. Tel.: +1 814 865 0036.
E-mail address: atm2@psu.edu (A.T. Motta).

0022-3115/$ - see front matter © 2007 Elsevier B.V. All rights reserved.
doi:10.1016/j.jnucmat.2007.05.022

required fuel enrichment and greater core design flexibility. Zr alloys could also be used for the water rods, proposed for these reactors. The use of Zr alloys for such rods would be easier to achieve because in the absence of heat flux, the peak cladding temperatures would be approximately equal to the average coolant outlet temperature. As part of a research program to assess the corrosion behavior of Zr alloys under supercritical water (SCW), we have performed extensive corrosion testing of model Zr alloys under SCW, followed by oxide characterization using various means. The results of this corrosion testing as well as initial characterization of the oxide layers using various techniques are reported in this work. These results are discussed in terms of the mechanisms governing the creation of a stable protective oxide in Zr alloys.

2. Experimental methods

The model alloys were prepared by arc-melting, re-melting at least four times to promote chemical homogeneity. The arc-melted ingots were beta-solution treated at 1050 °C for 30 min in a vacuum furnace, hot-rolled after pre-heating at temperatures ranging from 580 to 720 °C for 10 min and cold-rolled three times to a final thickness of 0.8 mm. Between the rolling steps, the cold-rolled sheets were intermediate-annealed at 580–720 °C depending on the alloy system.

Table 1 lists the alloys prepared and used in this study, and the target compositions. The actual compositions were measured and did not vary from the target composition by more than 10% (e.g. Zr1.0Fe, could vary by ±0.1Fe, to Zr0.9Fe or Zr1.1 Fe). The main groups contained alloys that form second phase particles (Zr–Fe–Cr alloys, Zr–Cr–Fe alloys, Zr–Cu–Mo) and alloys that form extensive solid solutions in alpha-Zr, (Zr–Nb, Zr–Sn and Zr–Nb–Sn) in addition to pure Zr and Zircaloy-4. The second phase particles formed were characterized using transmission electron microscopy and synchrotron radiation diffraction. This last technique has been shown to be able to detect very small amounts of second phase particles in Zr [6] and it was applied to all the samples studied. The phases encountered by indexing the diffraction patterns are shown in Table 1, as previously reported in [7].

Specimens for corrosion testing, measuring 25 by 20 by 0.8 mm, were cut from the manufactured strip, mechanically ground using 1200 grit SiC paper, and then pickled in a solution of 5 vol.% HF, 45 vol.% HNO_3 and 50 vol.% H_2O. The corrosion tests were conducted in 500 °C/1500 psi steam and 500 °C/3650 psi supercritical water (SCW) in a manner consistent with the ASTM Practice (G2-88). The corrosion behavior of the specimens was evaluated by measuring the weight gain as a function of the exposure time. The corrosion test in supercritical water was performed in two types of facilities: (i) a static autoclave (closed environment in which water does not recirculate) at Korean Atomic Energy Research Institute (KAERI) (designated as SCW static) and (ii) a dynamic loop system (water is constantly refreshed, and chemistry is controlled) at University of Michigan, both maintained at 500 °C 24.13 MPa (3500 psi) (designated as SCW dynamic). In the dynamical system, the water was continually cleaned and purified, such that inlet conductivity was kept below 0.1 μS/cm. Conductivity of the outlet water rose to 0.6 μS/cm. The oxygen content was <10 ppb and the flow rate was 12 l/m. The 500 °C steam corrosion test was performed at Westinghouse in a static autoclave at 10.34 MPa (1500 psi) (500 °C steam). In the static autoclaves also the water environment was deaerated, maintaining the oxygen content lower than 40 ppb.

Cross-sections of the oxides formed during autoclave exposures were prepared for successive examination by optical microscopy, micro-beam synchrotron radiation X-ray diffraction and fluorescence. The sample preparation procedure was described in detail in a previous publication [8]. Briefly, axial segments about 1.5-mm wide were cut from the corrosion samples. For each sample, two axial segments were bonded together with Gatan G-1 epoxy in such a manner that the oxide surfaces of interest (OD oxide for tubing) were adjacent and separated by only a thin layer of epoxy. These axial segments were inserted and contained in a thin-walled, 3-mm diameter brass tube with the same epoxy. After curing the epoxy, transverse slices about 0.5 mm thick were cut from the sample/tubing/epoxy composite. These slices were then mechanically ground and polished by use of progressively finer abrasive media to a thickness of about 0.1 mm. These disk-shaped samples were suitable for examination by micro-beam synchrotron radiation.

2.1. Synchrotron radiation experiments

Examination of the oxide layers was performed at the Advanced Photon Source (APS) at Argonne National Laboratory as described previously [8,9].

Table 1
Zr-based model alloys used in this study and their precipitate crystal structures, as determined by synchrotron radiation diffraction and transmission electron microscopy

Alloy system	Composition (wt%)	Precipitate crystal structure	Corrosion behavior in 500 °C SCW and steam
Zr–Nb	$x = 0.2$, 0.4, 1.0, 1.5, 2, 5%	*hcp* $Zr(Nb,Fe)_2$, *bcc* β-Nb and orthor. Zr_3Fe, except Zr0.2Nb, where no precipitates are present and only minor peaks in Zr0.4Nb	High rate, mostly protective, no breakaway except for Zr0.2Nb which shows immediate breakaway
ZrNbSn ZrSn	Zr0.4Nb0.4Sn and Zr0.4Nb0.2Sn Zr0.4Sn, Zr1.2Sn	Similar to 0.4Nb No precipitates	Higher rate than ZrNb Non-protective, nodular corrosion
Zr–Fe–Cr	Zr–0.4Fe–0.2Cr and Zr–0.2Fe–0.1Cr (two processing temperatures: 580 °C (L) and 720 °C (H)) Zr–1.0Fe–0.5Cr Zr0.6Fe–0.3Cr	Cubic C15 (low processing temperature) and hex. C14 (high processing temperature) $Zr(Cr,Fe)_2$	Protective behavior, low rates, stable oxide growth for alloying content $\geqslant 0.6\%$ No-protective breakaway behavior for alloying content $<0.6\%$
Zr–Cr–Fe	Zr0.5Cr, Zr–0.5Cr–0.2Fe, Zr–1.0Cr, Zr–1.0Cr–0.2Fe	Cubic $ZrCr_2$ and cubic $Zr(Cr,Fe)_2$	1.0Cr0.2Fe shows protective behavior, low rates, stable oxide growth. Others are mostly non-protective although 0.5Cr0.2Fe survived one SCW test
Zr–Fe–M	Zr–0.6Fe Zr0.6Fe–0.6Nb Zr0.6Fe–0.3Mo Zr1.0Fe	Orthor. Zr_3Fe β-Nb + hcp ZrNbFe Cubic $ZrMo_2$ and Ortho Zr_3Fe Orthor. Zr_3Fe	Limited testing (steam), protective behavior, low rates, stable oxide growth
Zr–Cr–M	Zr–1.0Cr–0.5Fe Zr1.0Cr–0.5Mo	C14 hex. $Zr(Cr,Fe)_2$ Cubic $ZrCr_2$	Protective behavior, low rates, stable oxide growth, Mo is detrimental
Zr–Cu–Mo	Zr–0.5Cu, Zr–0.5Cu–0.5Mo Zr–1.0Cu, Zr–1.0Cu–0.5Mo	Tet. Zr_2Cu and cubic $ZrMo_2$ when Mo present	High rate, mostly protective, no breakaway, lower alloying content is non-protective, and Mo is detrimental
Reference alloys	Sponge Zr, crystal bar Zr, Zircaloy-4	No precipitates for pure Zr hcp C14 $Zr(Cr,Fe)_2$ for Zircaloy-4	Non-protective, immediate breakaway corrosion

Two types of diffraction and fluorescence experiments were conducted: one in cross-section using a microbeam and one in frontal geometry to determine overall oxide texture.

In the cross-section experiments the beam that was used was focused to a size of 0.25 μm in the vertical direction (normal to the oxide–metal interface) and had a 2 μm footprint in the horizontal direction (parallel to the oxide–metal interface). The beam energy was 9.5 keV, corresponding to a wavelength of 0.1305 nm. Diffraction and fluorescence data were simultaneously collected from the sample as it was translated across the beam in step sizes ranging from 0.15 μm to 0.50 μm. The diffraction data were collected by a flat two-dimensional detector (CCD camera), while the fluorescence data were collected by an energy dispersive detector.

The positions of the oxide–metal and oxide–water interfaces were determined by monitoring Zr L line fluorescence counts as the sample was translated across the beam. The distance between the oxide–metal interface and the oxide-water interface measured by this method was in good agreement, to within 0.5 μm, with the optical determination of the oxide thickness. To obtain quantitative diffraction data, the digital data obtained from the two-dimensional detector were integrated over the elliptical sections for a fixed azimuthal angle, and the appropriate Lorentz and polarization correction factors were applied [8] to obtain a plot of diffracted intensity versus two-theta angle at each location analyzed.

The objective of the frontal texture experiment was to determine the orientation of the oxide layers formed on model alloys and to show the differences on the orientations of protective and non-protective oxide layers and it is described in Section 3.

2.2. Mechanical testing

To obtain data on mechanical properties on the model alloys in this study, tensile tests were performed both at room temperature and at 500 °C in accordance with the standard ASTM E8. The thickness of the sheet specimens for the tensile test was about 1.0 mm. The specimens were machined to be about 3.0 mm in width and 12.5 mm in the nominal gage length. The tensile tests were carried out at room temperature with the strain rate 8.3×10^{-5} s^{-1} through yield stress and 8.3×10^{-3} s^{-1} after yield stress to failure. The tensile tests at 500 °C were performed under 10^{-2} torr vacuum environment at a strain rate 8.3×10^{-4} s^{-1}to failure.

3. Experimental results

3.1. Corrosion weight gain

This section summarizes in quantitative terms (weight gain and corrosion rate) the corrosion results obtained. The main points are that:

(i) The corrosion rate was higher at 500 °C than at 360 °C, as expected. The percentage of the alloys exhibiting unstable oxide growth (or breakaway corrosion) also increased with temperature.
(ii) A wide variety of corrosion behaviors were observed for different alloys. Very minor changes in alloying content caused significant differences in corrosion behavior. Some alloys showed stable oxide growth with protective behavior to the end of the corrosion testing time, while some exhibited unstable oxide growth, including nodular corrosion and spallation.
(iii) Similar tendencies were observed in terms of breakaway susceptibility and corrosion rate ranking (i.e. the alloys that exhibit low corrosion rates at low temperature also tend to be among the lowest at high temperature).
(iv) A few of the alloys (Zircaloy-4, pure Zr) showed breakaway behavior right from the start. However, small alloying additions to pure Zr caused the corrosion behavior to become protective. A minimum of 0.6% alloying element was necessary to induce protective behavior.

More specific conclusions can be derived by the detailed examination of the corrosion results. We first show the illustrations of the main points above, and then discuss the results in more detail.

In general, the corrosion test results showed a range of corrosion behavior depending on the alloy composition. About half of the alloys studied showed poor, non-protective corrosion behavior, approximately ten alloys exhibited reasonable behavior (stable, protective oxide, but with higher rates) and six have shown excellent behavior (protective stable oxide, low rates, no breakaway).

Compared to similar corrosion tests conducted in the same alloys at 360 °C [10], the corrosion rates are much higher at 500 °C. Fig. 1 shows the comparison of the weight gains of a group of ZrFeCr alloys tested at both temperatures. The weight gains are about a factor of five higher at 500 °C than at 360 °C. For the best alloys, the oxide growth, however, remains stable and protective at high temperature, with the growth rate decreasing with increasing oxide thickness. Some tendencies can be observed: for both alloys the presence of Cr slightly improves corrosion behavior relative to pure ZrFe, and at both test temperatures the higher alloying content 1.0 Fe (relative to 0.6 Fe) slightly worsens behavior. The presence of Mo and Nb, in contrast, increases the corrosion rate relative to that of pure ZrFe. The ranking of alloys is the same at 360 °C compared to 500 °C.

Fig. 2 shows the corrosion weight gain in 500 °C steam for Zr0.2Fe0.1Cr and Zr0.4Fe0.2Cr, (low and high processing temperature). The results illustrate the point that alloys containing a total of less than about 0.6% alloying element content tended to exhibit unstable oxide growth in high temperature corrosion testing. While the corrosion rates of Zr0.4Fe0.2Cr showed stable protective oxide growth, the Zr0.2Fe0.1Cr alloys showed unstable behavior and higher corrosion rates. Further comments can be made regarding the role of precipitate size. The lower processing temperature alloys (containing smaller-size precipitates) showed better corrosion behavior than the high processing temperature alloys. In the Zr0.4Fe0.2Cr alloy, the higher processing temperature variant starts to exhibit unstable oxide growth around 60 days, while the low processing temperature alloy shows protective behavior up to 130 days exposure. For the Zr0.2Fe0.1Cr alloys, the higher processing temperature alloy exhibits immediate breakaway while the lower processing temperature alloy shows unstable oxide growth with spallation and mass loss. The better behavior exhibited by the alloys processed

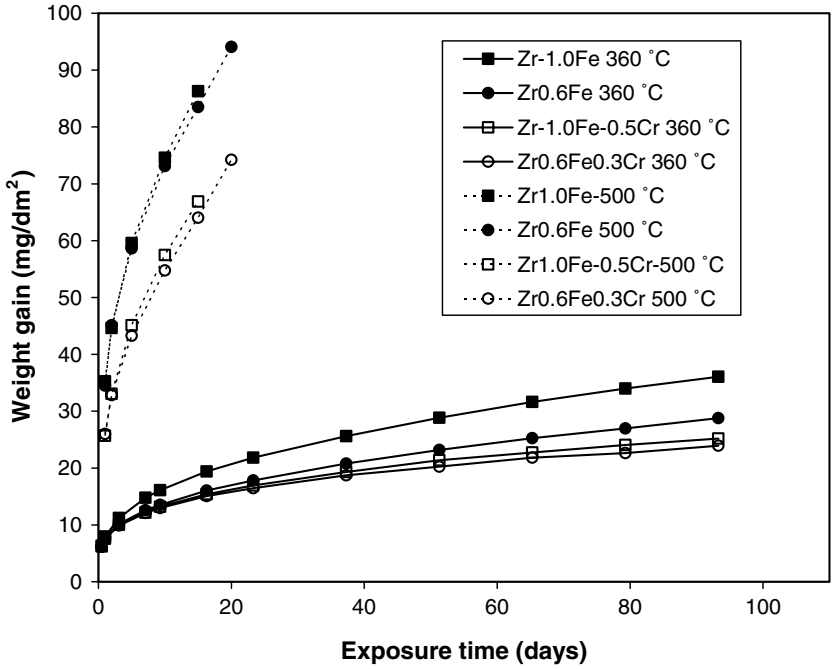

Fig. 1. Corrosion weight gain (mg/dm^2) versus exposure time (days) for ZrFeCr alloys tested in 360 °C water and in 500 °C steam.

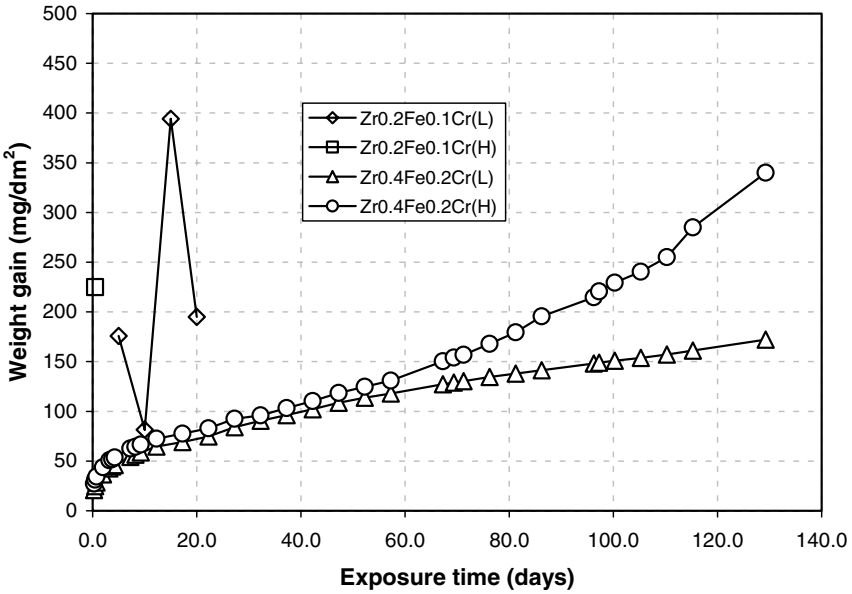

Fig. 2. Corrosion weight gain for ZrFeCr alloys in 500 °C steam.

at lower temperature (and thus with small precipitates) are in agreement with the better 360 °C nodular corrosion resistance exhibited by alloys with a smaller size precipitate distribution [11].

The solid solution alloys performed somewhat worse than the precipitate-based alloys, in general, during high temperature corrosion testing. Fig. 3 shows the weight gain for the Zr–Nb alloys and ZrNbSn alloys when tested in static supercritical water at KAERI. The most marked effect is from the absence of precipitates. The alloys whose alloying content is below the solubility limit (Zr0.2Nb and ZrSn alloys, which show no precipitates) show non-protective behavior. The Zr0.2Nb and the Zr–Sn alloys showed very high weight gains and unstable oxide growth, with the Zr–Sn alloys showing evidence of nodular corrosion. No marked difference is seen for various levels of Nb content

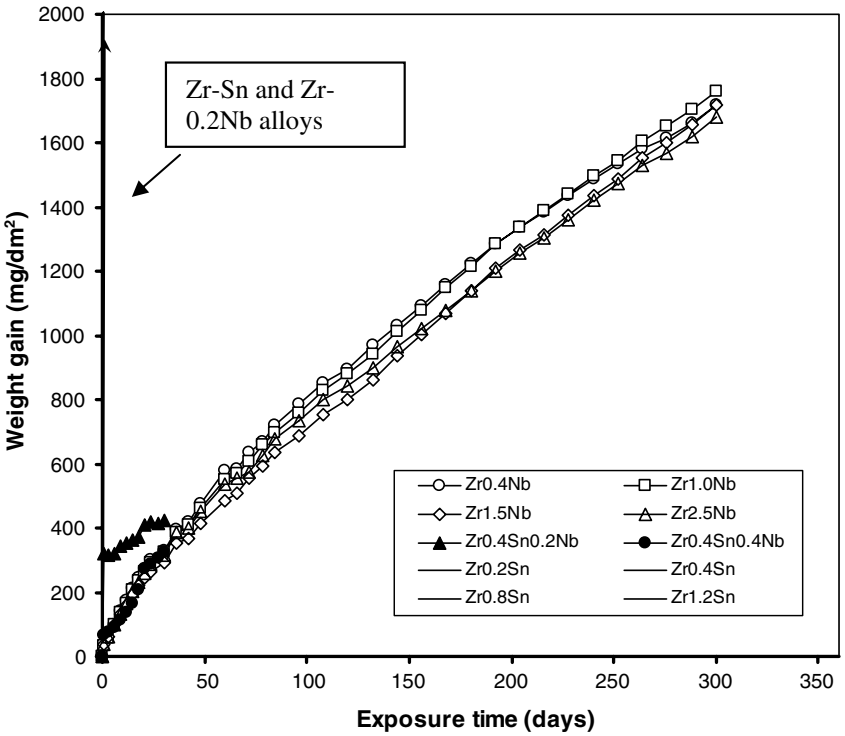

Fig. 3. Corrosion weight gain for ZrNb, ZrNbSn and ZrSn alloys tested in 500 °C supercritical water.

from 0.4 to 2.5%. Limited data exist for the NbSn alloys, but it appears the corrosion weight gain is higher than in the ZrNb alloys but lower than in ZrSn alloys. This suggests that precipitates have a specific role in the formation of protective oxides and that Sn is deleterious. Similar results were obtained in 500 °C steam testing of the same alloys in at KAERI.

A further point is that, unlike the behavior of, for example, Zircaloy-4, in 360 °C water, once the increases in corrosion rate take place, oxide protectiveness is normally not recovered. The degree of loss of protectiveness is also variable: for example alloy Zr0.5Cr0.2Fe shows a sudden increase in weight gain at 90 days, to a very high rate. At that point the oxide becomes whitish, and loses its protective nature, (this would be termed breakaway corrosion). This is in contrast to alloy Zr0.4Cr0.2Fe (H) alloy (Fig. 2) where the rate increases during corrosion but not catastrophically.

The weight gain w (mg/dm^2) during the initial protective regime can be characterized by a law of the type

$$w = At^n, \tag{1}$$

where t is the exposure time (days), n is a dimensionless constant, and A is a constant whose dimensions depend on the value of n. For each of the alloys tested, these constants were determined by least-squares fitting of the weight gain curves. The results were similar whether (a) individual sample weight gains were fitted and an average was calculated of the values of A and n obtained or (b) the average weight gain of all samples was fit as a single curve to obtain single average values of A and n. This is because for the alloys showing protective behavior there was not much variability in the weight gains of the various coupons. The calculated values of A and n are shown in Table 2.

Not much difference is seen in the calculated values of A and n at 500 °C among the different environments (steam, static SCW or dynamic SCW) for a given alloy. In general the values of A are much higher (30–35) than at 360 °C (which shows values of about 7–10) [10]. For the precipitate-based alloys the value of n is close to being cubic ($n = 0.33$) and is somewhat higher than the values calculated at 360 °C, which were on the order of 0.2–0.25. In contrast the Zr–Nb alloys exhibit a considerably higher value of n, near 0.66. The ZrFeNb alloy shows an intermediate value of n, at 0.43. Similar tendencies were observed in the calculations of the values of n for low temperature corrosion of the same alloys, i.e., the lowest values of n were for the ZrFeCr and ZrCrFe alloys and the highest for the ZrNb alloys, with intermediate values for

Table 2
Calculated values of A and n for the initial protective stage of the corrosion process

Alloy	Condition	A	n	$\bar{n}$
Zr0.4Fe0.2Cr (L)	SCW dynamic	32	0.34	0.32
	500 °C steam	31	0.29	
Zr–0.4Fe–0.2Cr (H)	SCW dynamic	32	0.36	
	500 °C steam	38	0.25	
	SCW static	35	0.36	
Zr–1.0Cr–0.2Fe	SCW dynamic	36	0.35	0.33
	500 °C steam	30	0.33	
	SCW static	30	0.30	
Zr–0.5Cr–0.2Fe	SCW dynamic	33	0.36	0.33
	500 °C steam	40	0.30	
Zr0.6Fe	500 °C steam	30	0.35	0.33
Zr0.6Fe0.3Cr		26	0.33	
Zr0.6Fe0.3Mo		38	0.30	
Zr1.0Fe	500 °C steam	35	0.33	0.35
Zr1.0Fe0.5Cr		26	0.35	
Zr1.0Cr0.5Fe		24	0.35	
Zr1.0Cr0.5Mo		24	0.36	
Zr0.6Fe0.6Nb	500 °C steam	32	0.43	0.43
Zr–0.4Nb	SCW static	30	0.71	0.67
Zr–1.0Nb		31	0.67	
Zr–1.5Nb		33	0.64	
Zr–2.5Nb		33	0.65	

mixtures of the two. This suggests that the alloying elements have an effect on the atomic transport in the oxide layer, likely by affecting the concentrations of oxygen vacancies that are responsible for transport of oxidizing species through the layer.

Fig. 4 shows the comparison of weight gains in the alloy Zr0.4Fe0.2Cr versus exposure time in static 500 °C steam and in 500 °C supercritical water (dynamic system). The results agree very well for both alloys: it is remarkable that not only do the weight gains agree, but so does the general shape of the curve and the time when it changes rate. This suggests that the effect of supercritical water compared to that of steam is less significant than the straightforward effect of temperature on corrosion rate. Results were consistent between static and dynamic autoclaves and showed a slightly higher rate in 500 °C SCW as compared to 500 °C steam. This suggests that static autoclave tests can be used to assess corrosion behavior at high temperature and that 500 °C steam tests can be used as an effective screening test [7].

Fig. 5 shows the weight gain versus exposure time for some of the tests conducted in this study, compared to those obtained for ferritic–martensitic and austenitic alloys also under consideration for the SCWR, tested in supercritical water containing 25 ppb oxygen [2]. It is apparent that the corrosion rates for the best Zr alloys are higher than those seen for austenitics and lower than those seen for ferritic–martensitic alloys. In addition, it appears that the oxide growth in the Zr alloys is more stable than in austenitic alloys (less incidence of weight loss or sudden weight changes). Fig. 5 also illustrates that the current Zr-based model alloys have been tested to much longer times than have the Fe-based alloys currently under consideration. It should be noted that although the results plotted

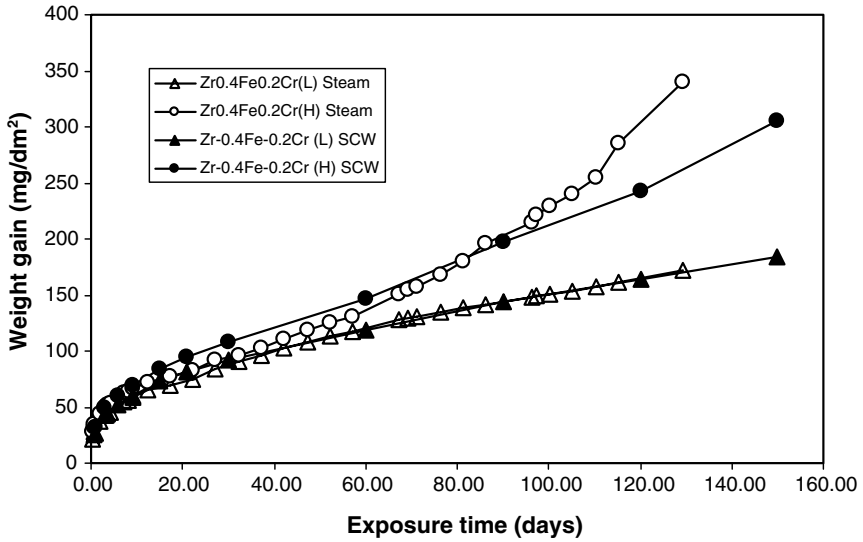

Fig. 4. Corrosion weight gain versus exposure time for high alloying content ZrFeCr alloys showing a comparison between tests in 500 °C supercritical water (filled symbols) and 500 °C steam (open symbols).

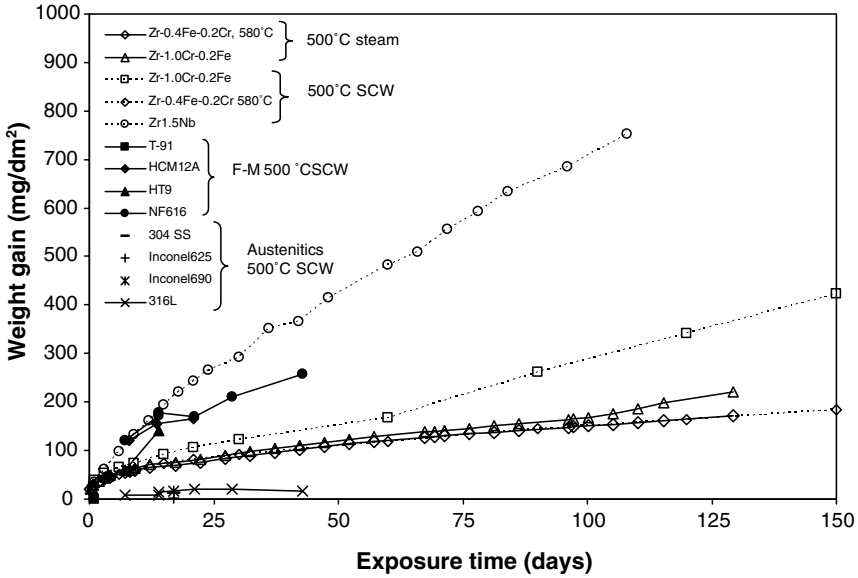

Fig. 5. Weight gain versus exposure time for some of the zirconium based model alloys tested in this program under different autoclave conditions (SCW or steam), as indicated. Also included are corrosion tests from ferritic–martensitic and austenitic alloys from other programs [2,23].

for the ferritic martensitic alloys and for the austenitic alloys are for tests conducted with 25 ppb oxygen the corresponding results for tests performed in deaerated supercritical water (<10 ppb oxygen) show very similar results.

The results suggest that the alloy composition and microstructure are predominant in determining corrosion behavior. In general, the best alloys were from the ZrFeCr system (which also behaved the best in a 360 °C water corrosion test). Higher alloying content (at least above 0.6%) improved corrosion resistance. The key to good corrosion resistance is to avoid breakaway corrosion and to foster the growth of a stable, protective oxide. The onset of breakaway often occurs after long exposure times, which indicates that short exposure tests may be inadequate for determining corrosion behavior at high temperature.

3.2. Characterization of oxides

To rationalize the differences in corrosion behavior, a concerted effort has been made to identify differences in oxide microstructure that can cause the differences in corrosion behavior. The oxide layers in protective and non-protective oxides have been examined with a variety of techniques, including scanning and transmission electron microscopy. Preliminary results from this oxide characterization are shown in this work.

Fig. 6 shows SEM micrographs of the oxide layers formed on some of the model alloys in this work. As mentioned previously, the thickness of the oxide film at each exposure period is consistent with the weight gain for the alloys exhibiting protective oxide growth, indicating that for these alloys no spallation or mass loss has occurred. Also for these alloys the oxide–metal interface is reasonably uniform (all alloys in Fig. 6 exhibit protective behavior, i.e. no weight gain kinetics breakaway). In contrast, preliminary examinations of the non-protective oxides show a more uneven oxide–metal interface. Fig. 6 shows an intermediate or 'diffusion' layer (arrowed) ahead of the advancing oxide. The diffraction pattern from synchrotron radiation shows strong Zr_3O peaks in a two to three micron region next to the oxide–metal interface, and lower intensity peaks 2–3 μm beyond that region, more or less corresponding to the region seen in SEM. Finally, as the oxide thickness increases, a greater incidence of lateral cracking in the oxide is observed, as expected. The thickest oxide layer alloys exhibits vertical cracking (Fig. 6(c)), which would provide easy access of the water to the fresh surface for additional corrosion.

It is noticeable that the oxide layers shown in Fig. 6 have a diffusion layer at the oxide–metal interface. Within that layer, EDX measurements show that the oxygen content drops from a constant value within the oxide proper down to near zero in the

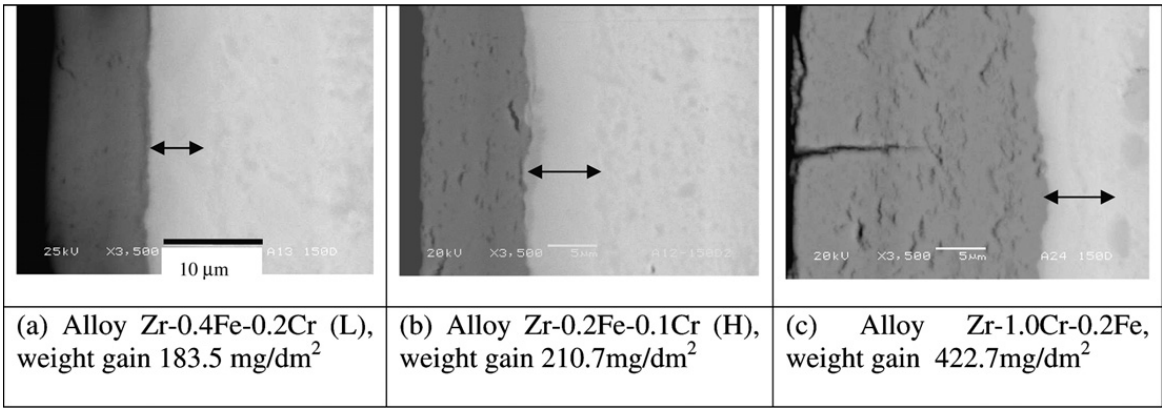

(a) Alloy Zr-0.4Fe-0.2Cr (L), weight gain 183.5 mg/dm^2

(b) Alloy Zr-0.2Fe-0.1Cr (H), weight gain 210.7mg/dm^2

(c) Alloy Zr-1.0Cr-0.2Fe, weight gain 422.7mg/dm^2

Fig. 6. Cross-sectional SEM images of oxides tested in 500 °C supercritical water to 150 days.

bulk of the metal. A similar diffusion layer has been observed in oxides formed in zirconium alloys at low temperature, in transmission electron microscopy both by imaging and by energy dispersive X-ray fluorescence [12]. The oxygen content was measured to be about 30%, or approximately equal to the solid solubility of oxygen into Zr [13]. The calculated weight gain of the samples submitted to SCW testing when translated into an oxide layer by assuming only ZrO_2 is formed (14.8 mg/dm^2 = 1 μm) does not correspond well either to the ZrO_2 layer or to the sum of the ZrO_2 layer and the inner layer. By assuming that the inner layer is a sub-oxide with an oxygen content of about 30%, the measured thickness agrees well with the weight gain. In the section below we show independent confirmation of this sub-oxide formation.

3.2.1. Microbeam synchrotron radiation diffraction

Using the experimental geometry described in Section 2 and in previous publications [8,9], diffraction patterns were obtained at successive locations in the metal, and through the oxide layer from the oxide–metal interface to the oxide–water interface. The diffraction patterns show which oxide, hydride and metal phases are present at various locations, and also yield information about their orientation relationships with the metal and among different oxide phases. The diffraction patterns are acquired about every 0.2 μm step across the oxide layer. One example of the collection of all such patterns for one sample is shown in Fig. 7, obtained from an oxide layer formed on a Zr1.0Cr0.2Fe sample after exposure to supercritical water in dynamic conditions for 150 days (this is the oxide layer shown in Fig. 6(c)).

Fig. 7 plots diffracted intensity versus two-theta angle versus position in the oxide layer. In Fig. 7, the interface is clearly defined by the appearance of several monoclinic oxide peaks, and the disappearance of the metal peaks. The position $x = 0$ corresponds to the oxide–metal interface, positive values of x correspond to positions in the oxide, and the negative values of x to positions in the metal. The oxides formed at 500 °C in supercritical water and in steam on the alloys Zr0.4Fe0.2Cr, both high and low processing temperature, Zr0.2Fe0.1Cr (H), Zr1.0Cr, Zr1.0Cr0.2Fe, Zr0.4Nb and Zr1.5Nb have been examined in the same way as shown in Fig. 7. The oxide structures in protective and non-protective oxides exhibit many similarities and some differences. For both protective and non-protective oxides, both monoclinic and tetragonal oxide phases are formed. In general, after the initial oxide formation the oxide develops in a columnar morphology, constituted principally of monoclinic oxide. The oxide growth direction in this case is near $(\bar{3}01)_M$. The ideal oxide growth direction is near the $(\bar{6}01)$monoclinic direction to reduce stress accumulation by optimizing the occupation of surface [14].

However, there are some notable differences, especially in the oxide–metal interface region. The structure of the oxide–metal interface is of great interest to understanding the mechanism of oxide growth and the differences between the protective and non-protective oxides. As can be seen by the arrowed peaks in Fig. 7, the protective alloys exhibit extra peaks in the diffraction scans obtained near the oxide–metal interface region. These peaks have been associated with two different phases found in that region in the protective oxides:

(i) A highly oriented tetragonal phase that has been hypothesized to be a crystallographic precursor of the monoclinic phase observed in the bulk of the oxide. The peak observed

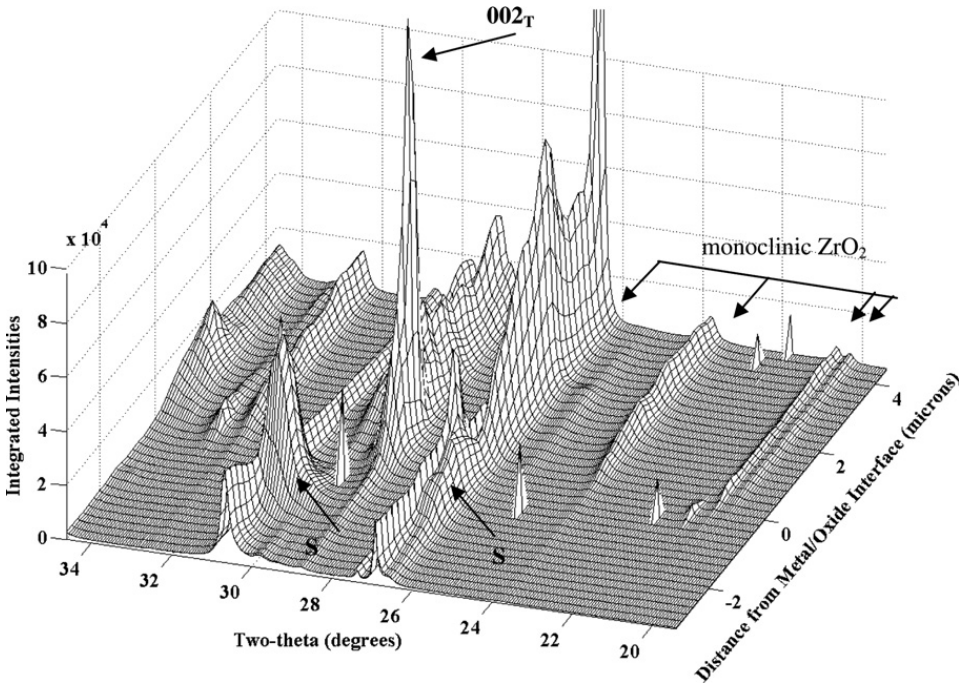

Fig. 7. Diffracted intensity (in arbitrary units) versus two-theta diffraction angle as a function of position in the oxide layer for alloy Zr–1.0Cr–0.2Fe, after exposure to 500 °C supercritical water for 150 days to a total weight gain of 422.7 mg/dm^2, which corresponds to an oxide thickness of about 20 μm. See text for explanation.

at the interface is the $[0\,0\,2]_T$ plane which has an orientation relationship with the $[0\,2\,0]_M$ plane, observed further away from the oxide metal interface, in the bulk of the oxide.

(ii) The sub-oxide phase Zr_3O (peaks indicated by S in Fig. 7, and which are shoulders on the low two-theta side of alpha-Zr metal peaks). This phase has also been seen at the oxide–metal interface by various researchers in oxides formed in Zr alloys at low temperature [15–20].

The Zr_3O sub-oxide peaks are seen in the region nearby the oxide–metal interface, appearing as shoulders on the lower two-theta side of the *hcp* Zr metal peaks ($[10\bar{1}0]$, $[10\bar{1}1]$ *hcp* peaks), as indicated by the arrows marked 'S' in Fig. 7. In this particular oxide the region exhibiting the sub-oxide peaks extends about 2–3 μm into the metal from the oxide–metal interface, in good agreement with the measured sub-oxide layer in SEM.

The diffraction peak at ~28.8 degrees two-theta, indexed as $[0\,0\,2]_T$ is the clearest indication of the highly oriented tetragonal phase. This peak has been observed in the examination of oxides formed during 360 °C pure water corrosion testing [9] in all the oxide layers that showed protective behavior, and is notably absent in the non-protective oxides formed at 360 °C. The most notable difference in the oxides formed at 500 °C compared to those formed at 360 °C is that the $[0\,0\,2]_T$ peak observed at the interface is much more intense. Preliminary indications appear to show that in the 500 °C oxides the intensity of this peak increases with the degree of protectiveness of this oxide. This is illustrated in Fig. 8. Fig. 8 shows a series blow-up of the diffraction lines across the oxide–metal interface for Zr–Nb alloys in samples cut into two different orientations and in two different alloys. These alloys showed protective behavior, but to a lesser degree than the Zr1.0Fe0.2Cr alloy shown in Fig. 7. The $[0\,0\,2]_T$ peak is still present, but is much lower than that observed in the alloy Zr1.0Fe0.2Cr, shown in Fig. 7.

The $[0\,0\,2]_T$ plane has been shown previously to align with the $[0\,2\,0]_M$ plane in the oxide and with the $[10\bar{1}0]$ *hcp* plane in the metal. Because in recrystallized material the $[11\bar{2}0]$ *hcp* planes align with the rolling direction of the sheet, most samples examined in this work have been prepared with the transverse direction perpendicular to the sample cross-section. In this orientation the $[10\bar{1}0]$ Zr plane is parallel to the sample surface, so that one would expect to observe the $[0\,0\,2]_T$ peak. This is also illustrated in Fig. 8. Fig. 8(a) shows samples oriented with the transverse direction perpendicular to the

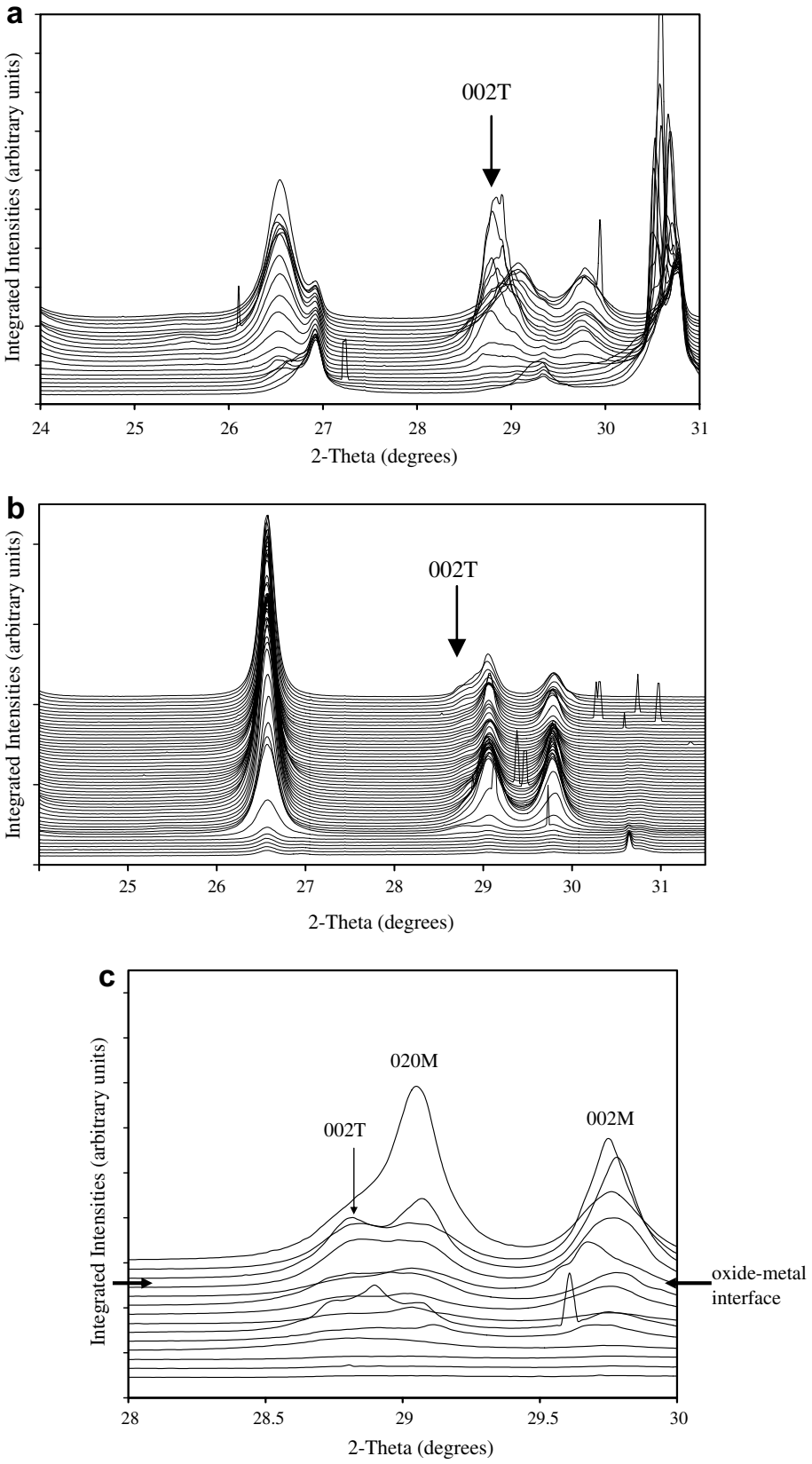

Fig. 8. Intensity versus two theta diffraction angle for the oxide–metal interface region in two oxide layers. (a) Zr1.5Nb exposed for 30 days in 500 °C steam (transverse direction normal to the sample surface), (b) Zr1.5Nb (same sample) with the rolling direction normal to the sample surface and (c) Zr0.4Nb with transverse direction normal to surface, after exposure to 300 days in supercritical water.

sample surface, showing that in this orientation the $[0\,0\,2]_T$ peak is quite visible. In contrast, Fig. 8(b) shows diffraction patterns taken from a sample with the rolling direction perpendicular to the sample surface, and in which the $[0\,0\,2]_T$ peak is not visible, confirming that it is indeed parallel to $[0\,2\,0]_M$ and to $[10\bar{1}0]$ *hcp*. Fig. 8(c) shows the same series of diffraction patterns taken for a sample surface perpendicular to the transverse direction for an oxide formed on the alloy Zr0.4Nb. This oxide is somewhat less protective than the oxide formed on Zr–1.5Nb and it has a correspondingly smaller $[0\,0\,2]_T$ peak.

3.2.2. Overall oxide texture

The overall texture differences between the protective and non-protective alloys were examined by determining the pole figures for various monoclinic oxide peaks. This was done using synchrotron radiation diffraction in frontal geometry, and collecting the data in an area detector, which allowed us to acquire several peaks simultaneously.

Diffraction patterns were collected on an image plate, using a 17 keV beam, incident at an angle of 3–4°. A schematic view of the experimental setup and data integration can be seen in Fig. 9. The sample was rotated around the sample normal (ω) by 5° from 0 to 200°, and for each rotation, one image was recorded. The recorded images were integrated along the diffraction rings by 5° sectors, effectively varying along the angle chi. Integrating along each ring we obtained pole figures for the peaks of interest (mostly monoclinic ZrO_2).

After integration, partial pole figures (0–360° phi, 0–70° chi) are obtained for various oxide and metal peaks. For the two-theta range we examined the pole figures can be obtained for the following poles: $[1\,1\,0]_M$, $[0\,1\,1]_M$, $[\bar{1}\,1\,1]_M$, $[1\,1\,1]_M$. The $\{2\,0\,0\}_M$ family is also available, but the peaks often overlap with each other and with other peaks from metal phases. Nevertheless, especially for the peaks that stand on their own, pole figures can be obtained for all peaks in the chosen two-theta range, with a single data collection.

In many ways the similarities in oxide texture for protective and non-protective oxides are greater than the differences. For both oxides, the oxide growth direction is close to the $\bar{6}01$ monoclinic oxide direction and the degree of orientation in that direction is similar (this was measured by calculating the resolved fraction of these poles along the growth direction of the oxide, analogously to the Kearns factor in Zr alloys [21]). Also for both types of oxides, the $\{\bar{1}11\}_M$ planes show two lobes oriented with their normals (poles) along the transverse × normal plane of the metal, and about 40–45° from the oxide growth direction. The difference is that the $[\bar{1}11]_M$ diffraction lobes exhibit about the same intensity (and are less localized) in the protective oxides and significantly skewed (one lobe stronger than the other) in the non-protective oxides. The $[2\,0\,0]_M$ pole figure also shows two lobes oriented about 10° from the oxide growth direction. In the protective oxides, the $(2\,0\,0)_M$ planes oriented with their normals along the transverse-normal plane of the metal and exhibit about the same intensity on the two diffraction lobes. However, in non-protective oxides, the $(2\,0\,0)_M$ planes also exhibit the intensity on one lobe stronger than the other.

This is demonstrated in Fig. 10 which shows the pole figures obtained using synchrotron radiation diffraction for two oxides formed at high temperature, one protective and one non-protective oxide. The two oxides are formed on Zr0.5Cr in 500 °C steam (non-protective oxide) and Zr1.0Cr0.2Fe in supercritical water which forms a protective oxide. The $[\bar{3}01]_M$ pole is not available in the two-theta range examined, but the $[\bar{2}01]_M$ pole is, and it stands not too far from the $[\bar{3}01]_M$, so that can serve as a proxy for that pole.

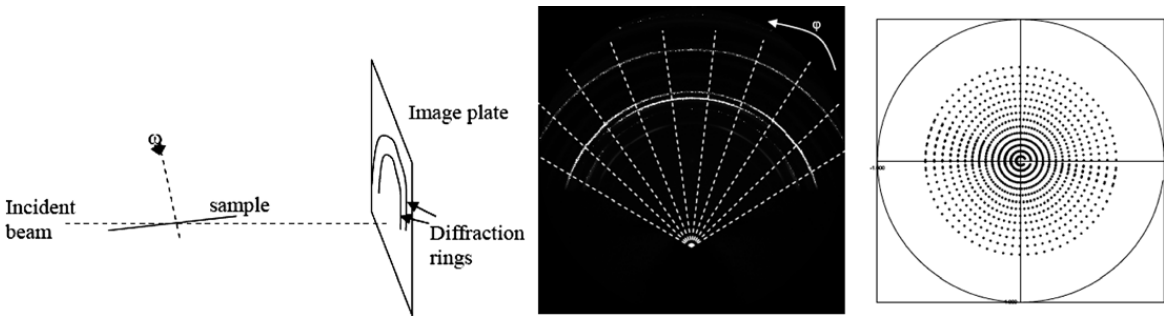

Fig. 9. Schematic experimental setup for pole figure acquisition and data integration.

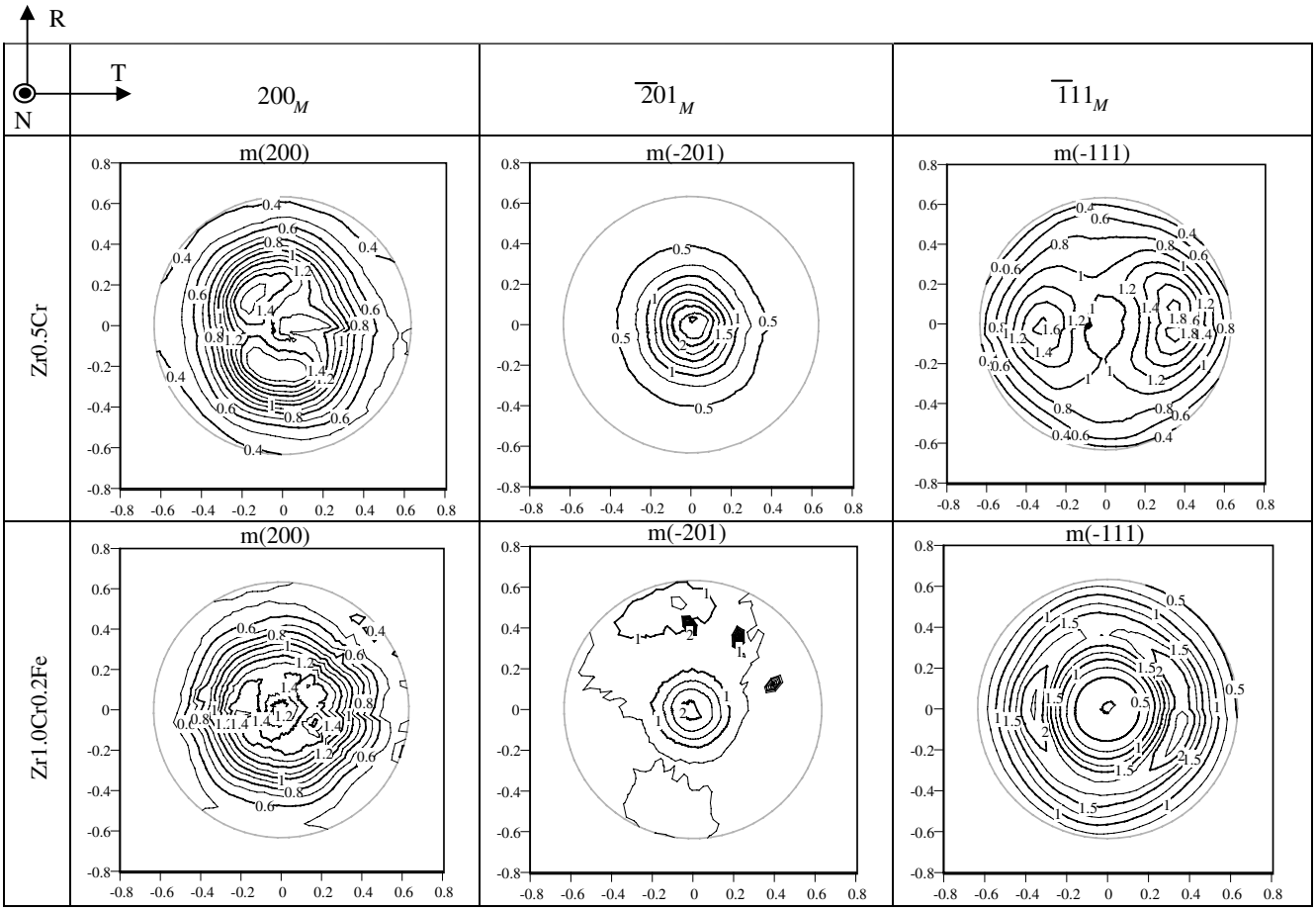

Fig. 10. Pole Figures for the ZrO_2 monoclinic peaks indicated, obtained averaged over the oxide layer, in frontal geometry for two oxides, one non-protective (Zr0.5Cr) and one protective (Zr1.0Fe0.2Cr). These figures are normalized such that the level '1' corresponds to the average intensity.

Fig. 10 shows that both oxides form with the growth direction aligned close to $[\bar{2}01]_M$ (and thus close to $\bar{3}01$), as the intensities of the $[\bar{2}01]_M$ pole figure are maximum close to the normal direction (i.e. the growth direction). The intensities of the $[\bar{1}11]_M$ poles are mostly aligned in the TN plane, about 40–45° from the normal (more so for the Zr0.5Cr non-protective oxide than for the Zr1.0Cr0.2Fe protective oxide). This results from the previously determined orientation relationship $[200]_M \| [0002]hcp$ and $[020]_M \| [10\bar{1}0]hcp$ [22]. It was a common observation in the non-protective oxides that one of the $[\bar{1}11]_M$ lobes was systematically stronger than the other. This may indicate that during non-protective oxide growth, the balance between the possible variants of growth that obey the orientation relationship above is perturbed, so that colonies of grains in one orientation dominate. In the protective oxide in contrast, the $[\bar{1}11]_M$ intensities are less concentrated in the TN plane and are more evenly distributed also. A corresponding imbalance is seen in the $[200]_M$ peak, which in the top left part of Fig. 10 shows a higher intensity to the left of normal (whereas the $[\bar{1}11]_M$ is right of the normal). Whether the unequal distribution of intensities between possible $[\bar{1}11]_M$ orientations is a cause or an effect of the oxide lack of protectiveness is open to question.

3.2.3. Mechanical properties

Fig. 11 shows the UTS and elongation of Zr–1.0X alloys. At room temperature, Zr–1.0Cu alloy has higher UTS than Zr–1.0Nb alloy and Zr–1.0Cu–0.5Mo alloy has higher UTS than Zr–1.0Cu alloy likely due to alloying effect on tensile strength. Zr–1.0Cr–0.2Fe alloy has the highest UTS among the alloys tested. At 500 °C, however, the strength of the alloys shows little correlation with composition because the hardening effect of alloying element almost disappears in the high temperature. A typical UTS of F–M steel is 640 MPa at room temperature and 425 MPa at 500 °C. In general, the addition of

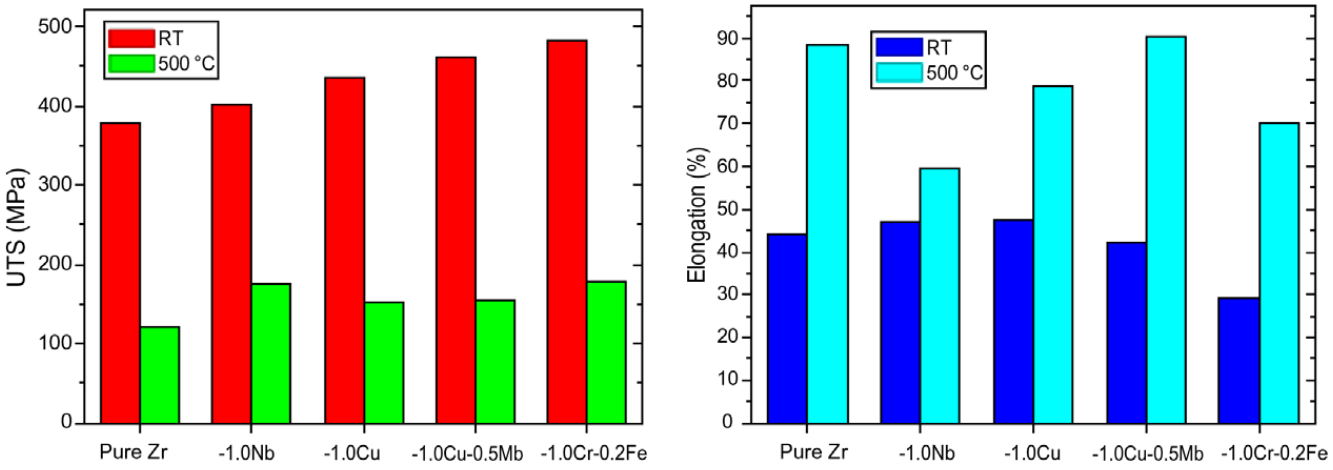

Fig. 11. Ultimate tensile strength and ductility for various model alloys, tested at room temperature and at 500 °C.

alloying elements to the model alloys increased their strength and decreased their elongation. The total elongation of F–M steel is 20% at room temperature and 17.5% at 500 °C, whereas that of the model alloys was 30–40% at room temperature and over 60% at 500 °C. Thus, the model alloys show reasonable ductility, but limited strength.

The mechanical properties of the model alloys were studied using tensile tests and hardness tests. The results show a significant decrease in strength with temperature, as expected. This will be an important issue in determining the ability of the reactor designers to use these alloys for load bearing components in the SCWR. An additional issue is the impact of hydrogen pickup from the corrosion process on the material ductility. Although there are indications that the hydrogen effect on mechanical properties is less severe at temperatures above 400–450 °C than at temperatures below 300 °C, with a higher hydrogen content there would still be concerns with handling issues after cooldown.

4. Conclusions

A detailed study has been conducted to address the issue of susceptibility of Zr alloys to uniform corrosion in the proposed supercritical water reactor. Thirty model alloys were corrosion tested for periods from 150 up to 400 days in 500 °C supercritical water and a wide range of corrosion behavior was observed.

1. Several alloys exhibited protective behavior throughout the test. The corrosion rate in these alloys was considerably higher than at 360 °C, but oxide growth was stable and protective. The best alloys contained Zr–Fe–Cr and had the compositions Zr0.4Fe0.2Cr and Zr1.0Cr0.2Fe. These were also the best alloys during corrosion testing at 360 °C.
2. The general agreement between the three high temperature tests was quite good. In particular little difference was seen between the results from static and dynamic autoclave testing. The results from lower pressure static testing agreed with the supercritical water results but showed slightly less oxide growth. Since the rankings of the alloys were preserved from test to test, it is possible the steam test could serve as a preliminary screening test for supercritical water behavior.
3. Fitting of the weight gain curves for the protective oxide alloys in the region of protective behavior showed nearly cubic behavior for the most protective alloys and supra-linear behavior ($n = 0.67$) for the Zr–Nb alloys. Overall, the oxidation rate of the best Zr alloys at 500 °C is lower than those of the best F–M alloys by about a factor of 2.

The oxides were also characterized to determine the oxide structures associated with protective and non-protective behavior and the preliminary conclusions are:

4. Characteristic differences exist in the oxide–metal interface regions of protective as compared to non-protective oxides. In particular the presence of two interfacial oxide phases, a highly oriented tetragonal phase and a sub-oxide phase was associated with protective behavior uniform corrosion.
5. The overall crystallographic texture of oxides also showed clear differences between protective and non-protective oxides. The growth direction of

the oxides was similar but the distribution of the lobes was considerably more anisotropic in the non-protective oxides than in the protective ones.

6. The strength of the model alloys studied decreases significantly between 360 and 500 °C. Typical strengths for the model alloys are 150 MPa at 500 °C. The ductility of the model alloys is significant at 500 °C.
7. Significant concerns exist in terms of creep rates, and other properties, but this research indicates that proper alloying additions induce protective oxide growth in model Zr alloys, such that from the corrosion point of view they should be considered as possible candidate materials for application in the supercritical water reactor.

Acknowledgements

The authors would like to thank Z. Cai, Y. Chu, J. Ilavsky and B. Lai at Argonne National Laboratory for their assistance with the experiments at APS. This research was supported by a DOE I-NERI grant no. DE-FG07-03RL14530 and by MOST at KAERI. Use of the Advanced Photon Source was supported by the US Department of Energy, Basic Energy Sciences, Office of Science, under Contract No. W-31-109-Eng-38. M.J. Gomes da Silva was a recipient of a scholarship from CNPq-Brazil for his doctoral study, while working on this project.

References

[1] A Technology Roadmap for GenIV Nuclear Technology Systems, <http://gif.inel.gov/roadmap/pdfs/gen_iv_roadmap.pdf>: US DOE Nuclear Energy Research Advisory Committee, 2002.
[2] G.S. Was, T.R. Allen, Time, Temperature, and Dissolved Oxygen Dependence of Oxidation in Austenitic and Ferritic–Martensitic Alloys in Supercritical Water, International Congress on Advances in Nuclear Power Plants, Seoul, Korea, 2005.
[3] J. Bolton, in: Corrosion of Reactor Materials II, IAEA, Vienna, 1962, p. 133.
[4] E. Gulbransen, K.F. Andrew, Electrochem. Technol. 4 (1966) 99.
[5] H.H. Klepfer, D.L. Douglass, ASTM STP 368 (1964) 118.
[6] K.T. Erwin, O. Delaire, A.T. Motta, R.C. Birtcher, Y. Chu, D. Mancini, J. Nucl. Mater. 294 (2001) 299.
[7] Y.H. Jeong, J.Y. Park, H.G. Kim, J.T. Busby, E.L. Gartner, M. Atzmon, G.S. Was, R. Comstock, M. Silva, A.T. Motta, in: Proceedings of the 12th International Conference on Environmental Degradation of Materials in Nuclear Power Systems – Water Reactors, 1369–1377. Snowbird, UT, TMS, 2005.
[8] A. Yilmazbayhan, A.T. Motta, R.J. Comstock, G.P. Sabol, B. Lai, Z. Cai, J. Nucl. Mater. 324 (2004) 6.
[9] A.T. Motta, A. Yilmazbayhan, R.J. Comstock, J. Partezana, G.P. Sabol, Z. Cai, B. Lai, J. ASTM Int. vol. 2 (2005) Paper # JAI 12375.
[10] A. Yilmazbayhan, A.T. Motta, H.G.Kim, Y.H. Jeong, J.Y. Park, R. Comstock, in: Proceedings of the 12th International Conference on Environmental Degradation of Materials in Nuclear Power Systems – Water Reactors, 201–210, Snowbird, Utah, TMS, 2005.
[11] F. Garzarolli, H. Stehle, Behavior of Structural Materials for Fuel and Control Elements in Light Water Reactor Cooled Power Reactors, IAEA IAEA-STI/Pub 721, 1987.
[12] A. Yilmazbayhan, E. Breval, A. Motta, R. Comstock, J. Nucl. Mater. 349 (2006) 265.
[13] Q. Peng, E. Gartner, J.T. Busby, A.T. Motta, G.S. Was, Corrosion 63 (6) (2007) 577.
[14] H. Li, H.M. Glavicic, J.A. Spuznar, Mater. Sci. Eng. A 366 (2004) 164.
[15] I.G. Ritchie, A. Atrens, J. Nucl. Mater. 67 (1977) 254.
[16] Yoshitaka Nishino, A.R. Krauss, Yuping Lin, D.M. Gruen, J. Nucl. Mater. 228 (1996) 346.
[17] C. Morant, J.M. Sanz, L. Galan, L. Soriano, F. Rueda, Vacuum 39 (1989) 860.
[18] M.C. Deibert, B.P. Thiesen, R. Kahraman, Appl. Surf. Sci. 35 (1989) 302.
[19] C.O. De Gonzalez, E.A. Garcia, Appl. Surf. Sci. 44 (1990) 211.
[20] T. Ericsson, G. Ostberg, B. Lehtinen, J. Nucl. Mater. 25 (1968) 322.
[21] J.J. Kearns, C.R. Woods, J. Nucl. Mater. 20 (1966) 241.
[22] A. Yilmazbayhan, Microstructural Basis of Uniform Corrosion in Zr Alloys, Ph.D. Thesis in Nuclear Engineering, 2004, Penn State University.
[23] G.S. Was, S. Teysseyre, J. McKinley, Corrosion and stress corrosion cracking of iron and Ni base austenitic alloys in supercritical water, Corrosion 2004, New Orleans, (2004), NACE International, paper # 4492.